

REPORT DOCUMENTATION PAGE			Form Approved OMB NO. 0704-0188		
<p>The public reporting burden for this collection of information is estimated to average 1 hour per response, including the time for reviewing instructions, searching existing data sources, gathering and maintaining the data needed, and completing and reviewing the collection of information. Send comments regarding this burden estimate or any other aspect of this collection of information, including suggestions for reducing this burden, to Washington Headquarters Services, Directorate for Information Operations and Reports, 1215 Jefferson Davis Highway, Suite 1204, Arlington VA, 22202-4302. Respondents should be aware that notwithstanding any other provision of law, no person shall be subject to any penalty for failing to comply with a collection of information if it does not display a currently valid OMB control number.</p> <p>PLEASE DO NOT RETURN YOUR FORM TO THE ABOVE ADDRESS.</p>					
1. REPORT DATE (DD-MM-YYYY)		2. REPORT TYPE New Reprint		3. DATES COVERED (From - To) -	
4. TITLE AND SUBTITLE Spherical nanoindentation study of the deformation micromechanisms of LiTaO <sub>3</sub> single crystals			5a. CONTRACT NUMBER W911NF-11-1-0525		
			5b. GRANT NUMBER		
			5c. PROGRAM ELEMENT NUMBER 611102		
6. AUTHORS Babak Anasori, Kurt. E. Sickafus, Igor. O. Usov, Michel W. Barsoum			5d. PROJECT NUMBER		
			5e. TASK NUMBER		
			5f. WORK UNIT NUMBER		
7. PERFORMING ORGANIZATION NAMES AND ADDRESSES Drexel University Office of Research Admin Drexel University Philadelphia, PA 19104 -			8. PERFORMING ORGANIZATION REPORT NUMBER		
9. SPONSORING/MONITORING AGENCY NAME(S) AND ADDRESS(ES) U.S. Army Research Office P.O. Box 12211 Research Triangle Park, NC 27709-2211			10. SPONSOR/MONITOR'S ACRONYM(S) ARO		
			11. SPONSOR/MONITOR'S REPORT NUMBER(S) 59692-MS.3		
12. DISTRIBUTION AVAILABILITY STATEMENT Approved for public release; distribution is unlimited.					
13. SUPPLEMENTARY NOTES The views, opinions and/or findings contained in this report are those of the author(s) and should not be construed as an official Department of the Army position, policy or decision, unless so designated by other documentation.					
14. ABSTRACT Herein, spherical nanoindentation (NI) was used to investigate the room temperature deformation behavior of C-plane LiTaO <sub>3</sub> single crystals loaded along the [0001] direction as a function of ion irradiation. When the NI load-displacement curves of 3 different nanoindenter radii (1.4 $\mu\text{m}$ , 5 $\mu\text{m}$ , and 21 $\mu\text{m}$ ) were converted to NI stress-strain curves, good agreement between them was found. The surface first deforms elastically – with a Young's modulus of 20565 GPa, calculated from					
15. SUBJECT TERMS Spherical Nanoindentation, Kinking Non-linear Elasticity					
16. SECURITY CLASSIFICATION OF:			17. LIMITATION OF ABSTRACT UU	15. NUMBER OF PAGES	19a. NAME OF RESPONSIBLE PERSON Michel Barsoum
a. REPORT UU	b. ABSTRACT UU	c. THIS PAGE UU			19b. TELEPHONE NUMBER 215-895-2338

## Report Title

Spherical nanoindentation study of the deformation micromechanisms of LiTaO<sub>3</sub> single crystals

### ABSTRACT

Herein, spherical nanoindentation (NI) was used to investigate the room temperature deformation behavior of C-plane LiTaO<sub>3</sub> single crystals loaded along the [0001] direction as a function of ion irradiation. When the NI load-displacement curves of 3 different nanoindenter radii (1.4  $\mu\text{m}$ , 5  $\mu\text{m}$ , and 21  $\mu\text{m}$ ) were converted to NI stress-strain curves, good agreement between them was found. The surface first deforms elastically – with a Young's modulus of 20565 GPa, calculated from the stiffness versus contact radii curves and 20763 GPa measured using a Berkovich tip – and then plastically deforms at  $\sim 6$  GPa. Repeated loading into the same location results in large, reproducible, fully reversible, nested hysteresis loops attributed to the formation of incipient kink bands (IKBs). The latter are coaxial fully reversible dislocation loops that spontaneously shrink when the load is removed. The IKBs most probably nucleate within the (10 $\bar{1}$ 2) twins that form near the surface. The sharper radii resulted in twin nucleation at lower stresses. The changes in the reversible loops' shape and areas can be related to the width of the twins that form. The latter were proportional to the nanoindenter tip radii and confirmed by scanning electron microscopy and by the fact that larger threshold stresses were needed for IKB nucleation with the smaller tip sizes. No effect of irradiation was observed on the NI response, presumably because of the mildness of the irradiation damage. VC 2011 American Institute of Physics.

---

**REPORT DOCUMENTATION PAGE (SF298)**  
**(Continuation Sheet)**

---

Continuation for Block 13

ARO Report Number    59692.3-MS  
Spherical nanoindentation study of the deformat    ...

Block 13: Supplementary Note

© 2011 . Published in Journal of Applied Physics, Vol. Ed. 0 110, (2) (2011), (, (2). DoD Components reserve a royalty-free, nonexclusive and irrevocable right to reproduce, publish, or otherwise use the work for Federal purposes, and to authroize others to do so (DODGARS §32.36). The views, opinions and/or findings contained in this report are those of the author(s) and should not be construed as an official Department of the Army position, policy or decision, unless so designated by other documentation.

Approved for public release; distribution is unlimited.

# Spherical nanoindentation study of the deformation micromechanisms of LiTaO<sub>3</sub> single crystals

B. Anasori,<sup>1,a)</sup> K. E. Sickafus,<sup>2</sup> I. O. Usov,<sup>2</sup> and M. W. Barsoum<sup>1</sup><sup>1</sup>*Department of Materials Science and Engineering, Drexel University, Philadelphia, Pennsylvania 19104, USA*<sup>2</sup>*Materials Science and Technology Division, Los Alamos National Laboratory, Los Alamos, New Mexico 87545, USA*

(Received 25 October 2010; accepted 28 May 2011; published online 25 July 2011)

Herein, spherical nanoindentation (NI) was used to investigate the room temperature deformation behavior of C-plane LiTaO<sub>3</sub> single crystals loaded along the [0001] direction as a function of ion irradiation. When the NI load-displacement curves of 3 different nanoindenter radii (1.4  $\mu\text{m}$ , 5  $\mu\text{m}$ , and 21  $\mu\text{m}$ ) were converted to NI stress-strain curves, good agreement between them was found. The surface first deforms elastically – with a Young's modulus of  $205 \pm 5$  GPa, calculated from the stiffness versus contact radii curves and  $207 \pm 3$  GPa measured using a Berkovich tip – and then plastically deforms at  $\approx 6$  GPa. Repeated loading into the same location results in large, reproducible, fully reversible, nested hysteresis loops attributed to the formation of incipient kink bands (IKBs). The latter are coaxial fully reversible dislocation loops that spontaneously shrink when the load is removed. The IKBs most probably nucleate within the (10 $\bar{1}$ 2) twins that form near the surface. The sharper radii resulted in twin nucleation at lower stresses. The changes in the reversible loops' shape and areas can be related to the width of the twins that form. The latter were proportional to the nanoindenter tip radii and confirmed by scanning electron microscopy and by the fact that larger threshold stresses were needed for IKB nucleation with the smaller tip sizes. No effect of irradiation was observed on the NI response, presumably because of the mildness of the irradiation damage. © 2011 American Institute of Physics. [doi:10.1063/1.3608158]

## I. INTRODUCTION

Lithium tantalate, LiTaO<sub>3</sub>, is one of the most attractive materials for nonlinear integrated optics. The properties of ferroelectric LiTaO<sub>3</sub> are similar to those of lithium niobate, LiNbO<sub>3</sub>, reviewed in detail elsewhere,<sup>1,2</sup> with excellent nonlinear optical properties, as well as higher thresholds to photorefractive damage than LiNbO<sub>3</sub> and a lower Curie temperature.<sup>3</sup> The importance of LiTaO<sub>3</sub> is emerging in applications, such as second-harmonic generation and optical parametric amplification/oscillation, because it can be processed to make waveguides and to engineer the nonlinearity through quasi-phase matching via periodic poling,<sup>4</sup> offering an important alternative to LiNbO<sub>3</sub> in devices for signal processing via quadratic cascading.<sup>5</sup> Despite these potential applications, little work has been carried out on its mechanical behavior, especially at room temperature. Doukhan *et al.*<sup>6</sup> described different lattice defects in LiTaO<sub>3</sub> and concluded, not surprisingly, that it had the same twinning system as LiNbO<sub>3</sub>.

Recently, we showed that the vast majority of plastically anisotropic solids with  $c/a$  ratios  $> 1.4$  can be classified as kinking nonlinear elastic (KNE) solids.<sup>7–10</sup> A sufficient condition for a solid to be KNE is plastic anisotropy. The signature of these solids is the formation of fully reversible, reproducible stress-strain loops during cyclic loading. The

full reversibility of these loops is believed to be caused by incipient kink bands (IKBs) that are comprised of multiple, coaxial, parallel dislocation loops (Fig. 1(a)), which remain extended only if the load is applied; when the load is removed, they shrink or are annihilated altogether.<sup>11</sup> At high stresses, such as under a nanoindenter, the IKBs sunder and devolve, first into mobile dislocation walls (MDW's) and ultimately into kink boundaries (KBs), which are irreversible (Fig. 1(b)).<sup>7,10,12–18</sup> On reloading to the same stress, IKBs nucleate in the newly created microdomains. The to-and-fro motion of the IKB dislocations, in turn, results in hysteresis and the dissipation of energy. Using this approach, we showed that graphite,<sup>18</sup> mica,<sup>7,17</sup> ZnO (C-orientation),<sup>12</sup> sapphire,<sup>13</sup> and GaN,<sup>14</sup> among many others, are KNE solids.

Following the pioneering work of Herbert *et al.*<sup>19</sup> and Oliver and Pharr,<sup>20</sup> Suganuma,<sup>21</sup> and Bushby,<sup>22</sup> we developed a technique for converting spherical NI load/displacement curves to NI stress/strain curves.<sup>23,24</sup> According to our technique, NI stress and strain are defined as  $P/\pi a^2$  and  $a/R$ , respectively, where  $P$ ,  $a$ , and  $R$  are load, contact radius, and tip radius. By plotting the NI stresses and strains, more information can be gleaned from the indentation results. We applied this method to better understand the deformation behavior of a number of oxide and nitride single crystals, such as sapphire,<sup>13</sup> ZnO,<sup>12</sup> LiNbO<sub>3</sub>,<sup>25</sup> mica,<sup>7,17</sup> GaN,<sup>14</sup> BaTiO<sub>3</sub>,<sup>26</sup> and, more recently, polycrystalline Y<sub>2</sub>O<sub>3</sub>.<sup>27</sup>

Most relevant to this paper is our recent work on the nanoindentation of C-plane LiNbO<sub>3</sub> single crystals loaded along [0001].<sup>25</sup> In that paper, we reported an elastic modulus

<sup>a)</sup>Author to whom correspondence should be addressed. Electronic mail: anasori@drexel.edu.

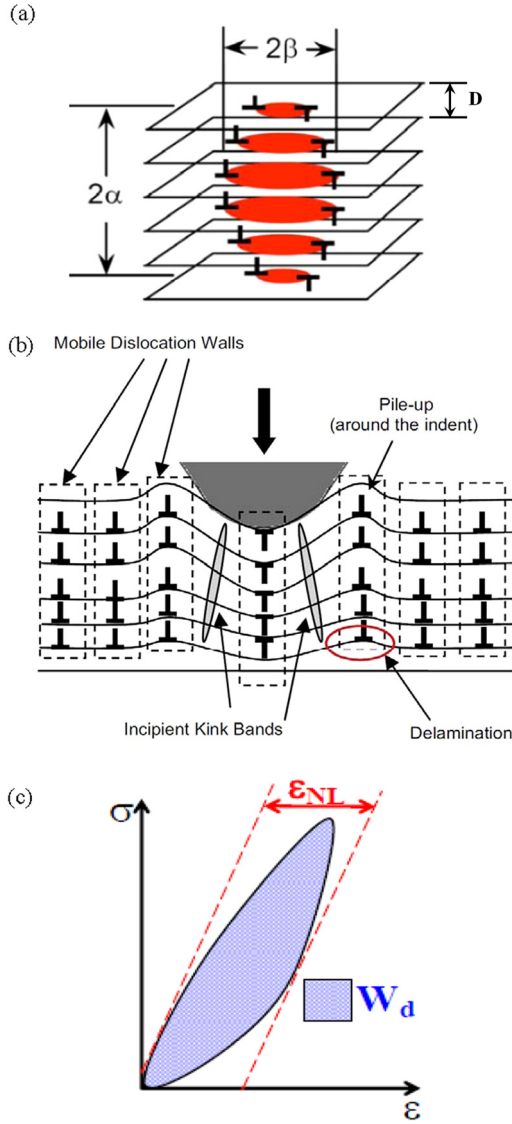


FIG. 1. (Color online) Schematic of (a) dislocation loops comprising an IKB; (b) schematic of what could be occurring below the indented surface. The emission of mobile dislocation walls that, in turn, form kink boundaries, are shown. Upon re-loading, the IKBs form within the kink boundaries or twins formed during the pop-in events. (c) Typical stress-strain curve for a KNE solid obtained under spherical nanoindentations, showing the definition of non-linear strain,  $\epsilon_{NL}$ , and the energy dissipated per unit volume per cycle,  $W_d$ .

of 186 GPa and a Vickers microhardness of about 4.5 GPa. Cyclic loading resulted in the signature of KNE solids, viz., large, fully reversible, reproducible, hysteretic stress-strain loops. As far as we are aware, these remain the largest ever reported for crystalline solids.

Before discussing the work carried out herein, it is important to summarize our IKB-based model that is, in turn, based on early work by Frank and Stroh (F & S).<sup>11</sup> The following is a simplified version. F & S considered an elliptic kink band (KB) with length,  $2\alpha$ , and width,  $2\beta$ , such that  $\alpha \gg \beta$  (Fig. 1(a)) and showed that the remote shear stress,  $\tau$ , needed to render such a subcritical KB unstable is given by

$$\tau_c \approx \frac{\sigma_t}{M} \approx \sqrt{\frac{4G^2 b \gamma_c}{\pi^2 2\alpha} \ln \frac{b}{w \gamma_c}}, \quad (1)$$

where  $\tau_c$  and  $\sigma_t$  are the remote critical shear and axial stresses, respectively.  $M$  is the Taylor factor relating the shear stress at the grain level to the applied stress. The maximum value of  $M$  is 2.  $G$ ,  $b$ , and  $w$  are, respectively, the shear modulus, Burgers vector, and a term related to the dislocation core width.<sup>11</sup> If one assumes that the local stress needed to nucleate an IKB is  $\approx G/35$ , then at 0.05 rad., the critical shear angle,  $\gamma_c$ , is small.<sup>11,28</sup>

As a first approximation, each dislocation loop (Fig. 1(a)) can be assumed to be comprised of two edge and two screw dislocation segments with lengths  $2\beta_x$  and  $2\beta_y$ , respectively. It is also assumed that, when  $\sigma > \sigma_t$ , the IKBs grow by increasing their width,  $2\beta$ , according to

$$2\beta_x \approx \frac{2\alpha(1-\nu)}{G\gamma_c} \frac{\sigma}{M}, \quad 2\beta_y \approx \frac{2\alpha}{G\gamma_c} \frac{\sigma}{M} \quad (2)$$

for the edge and screw components, respectively. It follows that, for  $\sigma > \sigma_t$ , the IKBs grow and the IKB-induced axial strain resulting from their growth is assumed to be given by<sup>29</sup>

$$\begin{aligned} \epsilon_{IKB} &= \frac{\Delta V N_k \gamma_c}{k_1} = \frac{N_k \gamma_c 4\pi\alpha(\beta_x \beta_y - \beta_{c,x} \beta_{c,y})}{3k_1} \\ &= \frac{4\pi(1-\nu)N_k \alpha^3}{3k_1 G^2 \gamma_c M^2} (\sigma^2 - \sigma_t^2) = m_1 (\sigma^2 - \sigma_t^2), \end{aligned} \quad (3)$$

where  $m_1$  is the coefficient before the term in brackets in the fourth term,  $N_k$  is the number of IKBs per unit volume, and  $\Delta V$  is the change in the volume kinked as the IKBs grow from a size at  $\sigma_t$  to their size at  $\sigma$ . The factor  $k_1$  relates the volumetric strain due to the IKBs to the axial strain along the loading direction. Experimentally,  $k_1$  varies from 1 to 2. For example, in polycrystalline Mg, it is closer to 1,<sup>30</sup> while in Co, it is closer to 2.<sup>31</sup> Reed-Hill *et al.*<sup>32</sup> also assumed  $k_1 = 2$  when they modeled twins in Zr. Herein, we assumed  $k_1 = 2$ ; the implications and ramifications of this assumption are discussed below. Once  $m_1$  is determined experimentally, if  $2\alpha$  can be estimated,  $N_k$  can be calculated. Note that  $N_k \alpha^3$  is of the order of unity.

If  $\Omega$  is the energy dissipated by a dislocation line sweeping a unit area, then the energy dissipated per cycle per unit volume,  $W_d$ , can be expressed as<sup>8,29</sup>

$$\begin{aligned} W_d &= \frac{4\Omega\pi N_k \alpha}{D} (\beta_x \beta_y - \beta_{c,x} \beta_{c,y}) = 3k_1 \frac{\Omega}{b} m_1 (\sigma^2 - \sigma_t^2) \\ &= m_2 (\sigma^2 - \sigma_t^2), \end{aligned} \quad (4)$$

in which  $D$  is the distance between dislocation loops along  $2\alpha$  (Fig. 1a). It follows that  $\Omega/b$  should be proportional, if not equal, to the critical resolved shear stress (CRSS) of an IKB dislocation loop. Combining Eqs. (3) and (4) yields

$$W_d = 3k_1 \frac{\Omega}{b} \epsilon_{IKB} = \frac{m_2}{m_1} \epsilon_{IKB}. \quad (5)$$

Figure 1(b) shows a schematic of how  $\epsilon_{NL}$  and  $W_d$  are estimated from the NI stress-strain curves.

Assuming the IKBs to be cylinders with radii  $\beta_{av}$ , then the reversible dislocation density,  $\rho_{rev}$ , due to the IKBs is given by

$$\rho_{rev} = \frac{2\pi N_k 2\alpha\beta_{av}}{D} = \frac{4\pi N_k \alpha\beta_{av}\gamma_c}{b}, \quad (6)$$

where  $\beta_{av}$  is the average of  $\beta_x$  and  $\beta_y$ .

Since IKBs are comprised of dislocation loops and NI is sensitive to near surface properties, it is reasonable to assume that any process that induces near surface defects could affect the NI response of KNE solids. This is particularly true since we recently showed that the average pop-in stresses in defective micas were significantly lower than those in less defective ones.<sup>17</sup> At this time, it is fairly well established that irradiation of solids with light ions, such as helium (He), can create a large number of defects, including vacancies and interstitials, voids, dislocation loops, and He bubbles, etc.<sup>33,34</sup> On the other hand, there are some parameters, such as the material's compositional complexity, that can act to suppress the nucleation and growth of dislocation loops and voids during irradiation.<sup>35</sup> LiTaO<sub>3</sub> belongs to a family of oxides that possess a corundum-derivative crystal structure<sup>36</sup> that, because of their compositional complexity, are considered to be radiation tolerant materials. LiTaO<sub>3</sub> is the least radiation tolerant in this family of oxides and is one reason it was chosen for this work.<sup>35</sup>

The aim of this paper is two-fold. The first is to understand the deformation micro-mechanisms of C-plane LiTaO<sub>3</sub> single crystals loaded along [0001]. The second is to explore the effects of He ion irradiation on the deformation mechanisms.

## II. EXPERIMENTAL DETAILS

Two high quality, (0001) or C-plane orientation, LiTaO<sub>3</sub> single crystals were purchased (Yamaju Ceramics Co., Aichi, Japan) with both sides polished to a mirror finish.

The NI experiments were performed at room temperature with a nanoindenter (XP system, MTS Corp., Oak Ridge, TN) equipped with a continuous stiffness measurement (CSM) attachment. Three diamond hemispherical indenters with radii,  $R$ , of 21  $\mu\text{m}$ , 5  $\mu\text{m}$ , and 1.4  $\mu\text{m}$  were used. Typically, a tip was repeatedly indented in the same location to a given load along [0001]. The loading rate/load ratio was constant at 0.1. To correct for instrumental drift, the unloading segments of the sixth and subsequent cycles were shifted so as to align them with the corresponding unloading segment of the previous cycles before the results were converted to NI stress-strain curves. This was carried out *if and only if* successive load-displacement cycles had identical areas (see below).

The load-displacement results were zero-point corrected. To determine the effective zero point, we used the method of Moseson *et al.*<sup>24</sup> The latter exploits the fact that, for a spherical tip, the following relationship:

$$S = 2E^*a, \quad (7)$$

where  $S$  and  $a$  are harmonic contact stiffness of the surface and contact radius, respectively, holds. More details can be found in Ref. 24. The effective modulus of the surface,  $E^*$  is given by

$$\frac{1}{E^*} = \frac{(1-\nu^2)}{E} + \frac{(1-0.07^2)}{1140}, \quad (8)$$

where  $\nu$  and  $E$  are the Poisson's ratio and Young's moduli of the sample, respectively. The other numbers are the corresponding values for the diamond indenter tip. Poisson's ratio of LiTaO<sub>3</sub> is assumed to be 0.25.<sup>37</sup>

Post-indentation surface features were examined using a scanning electron microscope (SEM; Zeiss Supra 50VP, Germany). The Vickers microhardness was measured using a load of 10 N. The moduli and hardness values were also measured using a Berkovich indenter and the Oliver and Pharr method.<sup>20</sup>

One of the LiTaO<sub>3</sub> crystals was irradiated with 2 MeV He<sup>+</sup> ions at room temperature to an ion fluence of  $1.67 \times 10^{15}$  He/cm<sup>2</sup>. Ion range, nuclear and electronic energy partitioning were estimated using Lindhard-Scharff-Schiott (LSS) procedure for calculating ion stopping.<sup>38-41</sup> Based on LSS, the range of 2 MeV He<sup>+</sup> ions in LiTaO<sub>3</sub> was estimated to be 4.81  $\mu\text{m}$  (assuming a mass density for LiTaO<sub>3</sub> of 7.41 g/cm<sup>3</sup>).

The lattice damage was measured by Rutherford backscattering spectroscopy (RBS) in channeling mode (RBS/C) using a 2 MeV He<sup>+</sup> ion beam with a backscattering angle of 167°. The ion irradiation and RBS/C analysis were carried out at the Ion Beam Materials Laboratory (IBML) at Los Alamos National Laboratory.

## III. RESULTS

### A. Nanoindentation results

Typical NI load-displacement results obtained when the 21  $\mu\text{m}$  radius tip is indented into the unirradiated sample are shown in Fig. 2. The corresponding results for the 5  $\mu\text{m}$  tip radius indenter are shown in the bottom right inset of the same figure. The results for the irradiated samples were identical to the unirradiated samples and are not shown.

In all load-displacement plots (Fig. 2), the first cycle was open. After the indenter was unloaded and reloaded to the same maximum load and into the same location, the repeat cycles close and ultimately become fully reversible

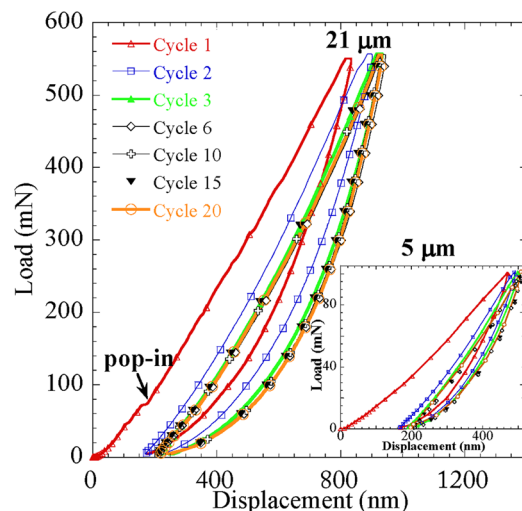


FIG. 2. (Color online) Typical NI load-displacement curves when an unirradiated C-plane LiTaO<sub>3</sub> single crystal is loaded 20 times to 550 mN with the 21  $\mu\text{m}$  radius indenter. Note presence of small pop-ins. Bottom right inset shows the same plot for the 5  $\mu\text{m}$  radius tip loaded twenty times to 100 mN. In both cases, for clarity's sake, only a few cycles are plotted.



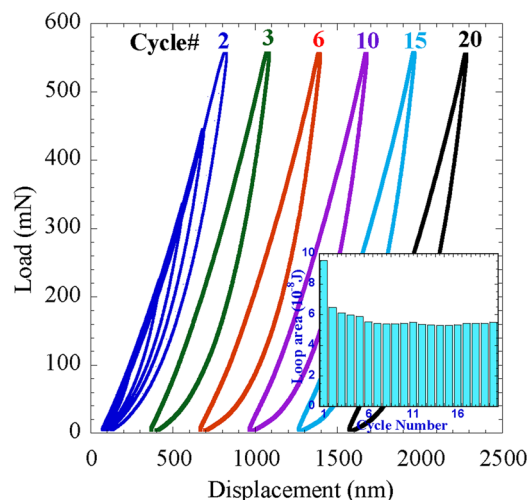


FIG. 3. (Color online) Load-displacement cycles 2, 3, 6, 10, 15, and 20 obtained when the  $21\ \mu\text{m}$  tip was indented along the  $[0001]$  into an irradiated surface. The curves were shifted to the right from their original position for clarity. Cycles 2 and 3 are open; cycles 6 to 20 are closed and equal in area. Re-loading to a lower load after loading to the maximal load always results in closed, reversible nested loops, shown for cycle 2 only. Inset plots the corresponding load-displacement loops' areas vs cycle number obtained with the  $21\ \mu\text{m}$  tip on an unirradiated surface. After about 6 cycles, the areas are constant.

and reproducible (Fig. 3). However, perfect reproducibility is only achieved somewhere between cycles 5 to 10 for all locations and tip sizes. The area of cycles 6 to 20 are, within the resolution limit of our NI, identical (inset in Fig. 3).

Typical nested loops obtained when a given location is loaded to a maximum load, unloaded, and re-loaded to progressively higher loads are shown on the loop labeled 2 in Fig. 3.

When the  $S$  versus  $a$  results for the three radii are plotted (Fig. 4(a)), it is obvious that the relationship between the two is linear. From least squares fits of the lines, and making use of Eqs. (7) and (8), the average Young's moduli for the  $1.4\ \mu\text{m}$ ,  $5\ \mu\text{m}$ , and  $21\ \mu\text{m}$  tips, were calculated to be  $206 \pm 4\ \text{GPa}$ ,  $205 \pm 5\ \text{GPa}$ , and  $220 \pm 5\ \text{GPa}$ , respectively. The former two values are in excellent agreement with the moduli obtained using a Berkovich tip on the same surface, viz.,  $207 \pm 3\ \text{GPa}$ .

Why  $E$  for the  $21\ \mu\text{m}$  tip is different is unclear at this time. One possibility for the discrepancy is that the  $21\ \mu\text{m}$  indenter tip may not be perfectly spherical. In the case of the  $5\ \mu\text{m}$  and  $1.4\ \mu\text{m}$  indenters, the total penetration depth was kept below the spherical limit, as reported by Albayrak *et al.*<sup>27</sup> Regardless of the reasons for these discrepancies, they have little bearing on the conclusions reached in this work that, as shown below, rely much more on the results obtained in the plastic and/or nonlinear elastic regimes for which what occurs in the elastic regime has little influence, since for all intents and purposes in the plastic regime,  $h_t \approx h_c$ , where  $h_t$  is the total indentation depth and  $h_c$  is the contact height.

Figure 4(b) compares the stress-strain curves for the three tips. In all cases, the first cycle delineates two regimes: a linear elastic regime followed by a plastic regime. For the  $1.4\ \mu\text{m}$  and  $5\ \mu\text{m}$  tips, the slope of the elastic regime (shown by a dashed inclined line), is consistent with the results of  $S$

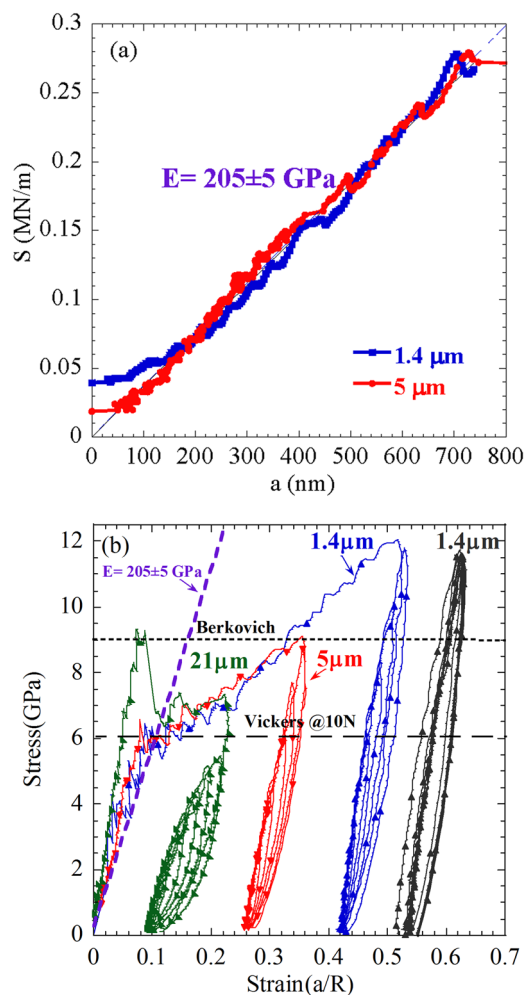


FIG. 4. (Color online) (a) The  $S$  vs  $a$  curves for the  $1.4\ \mu\text{m}$  and  $5\ \mu\text{m}$  tips. (b) Typical NI stress-strain curves obtained after a given location was indented to the highest loads (550 mN for  $21\ \mu\text{m}$ , 100 mN for  $5\ \mu\text{m}$ , and 20 mN for  $1.4\ \mu\text{m}$  tips) for two cycles, unloaded and progressively loaded to higher stresses to obtain the nested loops (three left curves). Plot shown on extreme right shows the reproducible NI stress-strain loops for  $1.4\ \mu\text{m}$  indenter; it was shifted to the right from its original position for clarity. Dashed horizontal and inclined lines represent the Vickers microhardness, Berkovich hardness, and elastic moduli obtained from the  $S$  vs  $a$  curves, respectively. Pop-ins were only observed when the  $21\ \mu\text{m}$  tip indenter was used.

versus  $a$  plots (Fig. 4(a)). As noted above, the stress-strain results for the  $21\ \mu\text{m}$  tip indenter in the elastic regime are incorrect.

During the first cycle, in the plastic regime, the strain-hardening rate is more or less constant. More importantly, in the plastic regime, the overall shapes of the stress-strain curves are weak functions of  $R$ . Relatively, large observable pop-in events between the elastic and plastic regimes were only observed when the  $21\ \mu\text{m}$  tip was used.

At  $\approx 6 \pm 0.5\ \text{GPa}$ , the Vickers microhardness values (denoted by a horizontal dashed line in Fig. 4(b)) were measured on both unirradiated and irradiated samples at a load of 10 N. At  $\approx 9\ \text{GPa}$ , the Berkovich hardness measured on the same surfaces is also shown as a horizontal dashed line.

In much of our work to date,<sup>7,12-14,17,18,25,26</sup> the deformation was initially linear up to a pop-in stress, beyond which the deformation was plastic. As noted above, herein,

no pop-ins were observed for the 1.4  $\mu\text{m}$  tip and only a few for the 5  $\mu\text{m}$  tip. Conversely, for the 21  $\mu\text{m}$  tip, a variation in pop-in stresses was observed. The distribution of pop-in stresses can be adequately described by Weibull statistics (Fig. 5) and appear not to be a function of irradiation.

After the first cycle, two loading trajectories were followed. The first was to load the same location 20 times to the maximum load. Such experiments were carried out to investigate the reproducibility and fully reversible nature of the loops generated. Based on the results shown in Fig. 4(b) and the loops shown on the extreme right, we conclude that these loops are highly reproducible and reversible.

The second protocol was to load the indenter to the highest load for two cycles, unload, and then reload to progressively higher loads to generate the nested loops observed in Fig. 4(b).<sup>8,9,25,42</sup> Here, as in previous work on  $\text{LiNbO}_3$ ,<sup>25</sup> the shape of the loops is dependent on  $R$ . The 21  $\mu\text{m}$  and 5  $\mu\text{m}$  indenters yield shorter, wider loops; the 1.4  $\mu\text{m}$  tip, on the other hand, results in elongated thinner loops (Fig. 4(b)).

All KNE solids can be characterized by three parameters,  $\sigma$ ,  $\varepsilon_{\text{NL}}$ , and  $W_d$ , all obtainable from the hysteretic stress-strain curves. At every stress,  $\sigma$ ,  $W_d$ , and  $\varepsilon_{\text{NL}}$  were estimated from the nested loops, (for how  $\varepsilon_{\text{NL}}$  is defined in this work, see Fig. 1(c)). According to Eqs. (4) and (5),  $W_d$  should scale with both  $\sigma^2$  and  $\varepsilon_{\text{NL}}$ , as observed in Figs. 6(a) and 6(b), respectively. The lowest correlation coefficient,  $\theta^2$ , obtained from least square analysis of the results-shown in Fig. 6 by the solid inclined lines-is 0.97; most are  $>0.98$ . It is obvious that the model predictions are well adhered to. The next step is to try and quantify some of the parameters to ensure that they are physically tenable. To do so, the following assumptions were made:  $G = c_{44} = 95$  GPa,<sup>43</sup>  $\nu = 0.25$ ,<sup>37</sup>  $\gamma = 0.05$ ,  $w = b = 0.515$  nm,<sup>44</sup>  $k_1 = 2$ , and  $M = 2$ . As noted above, experimentally for polycrystalline Mg,  $k_1$  was found to vary between 1 and 2.<sup>30,45,46</sup> For Co,  $k_1$  was estimated to be 2. Reed-Hill *et al.*<sup>32</sup> assumed  $k_1 = 2$  for  $(11\bar{2}1)$  twins in Zr. Given that the  $(11\bar{2}1)$  twin is a special case of a kink boundary, for which a dislocation loop is nucleated every  $c$ -lattice

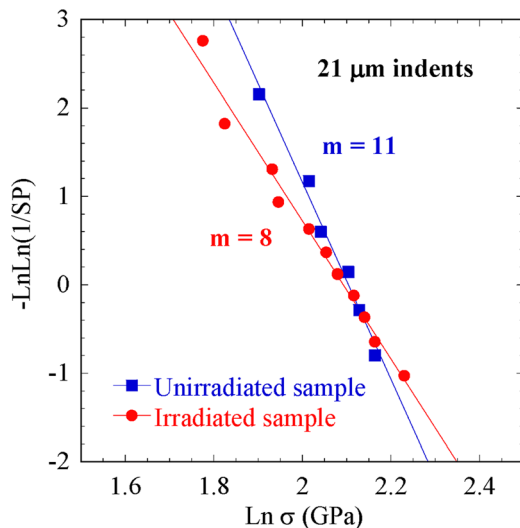


FIG. 5. (Color online) Plot of Weibull probabilities (SP) vs pop-in stresses ( $\sigma$ ) for 21  $\mu\text{m}$  indenter for both unirradiated and irradiated samples. The Weibull moduli,  $m$ , are shown on the figure.

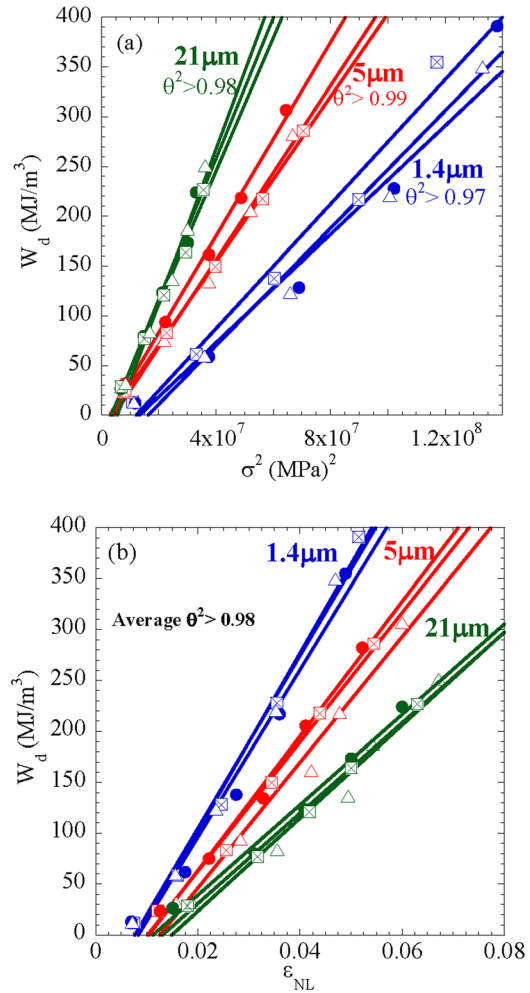


FIG. 6. (Color online) Plots of (a)  $W_d$  vs  $\sigma^2$  and (b)  $W_d$  vs  $\varepsilon_{\text{NL}}$  as a function of indenter radius. The slope dependence on the tip size is clear in (b). Each line represents a different location.

parameter, i.e.,  $D = c$ , it is reasonable to assume this value here as well.<sup>47</sup> This comment notwithstanding, the objective of this numerical exercise is not to obtain absolute and accurate values for, say, the CRSS's. The purpose is more to show that our model is consistent with the results obtained and can, in principle, explain them without resulting in values that are not physical. This is especially true here, given the very complex, non-uniform, state of stress under the nanoindenter and all the simplifying assumptions made.

According to our model, the x-axis intercepts of Fig. 6(a) represent the threshold stresses,  $\sigma_t$ , needed to nucleate the IKBs. Using these  $\sigma_t$  values and the assumptions made above, the lengths of the IKBs, or domain sizes,  $2\alpha$ , can be estimated from Eq. (1). Once  $2\alpha$  is known,  $2\beta_x$  and  $2\beta_y$ , at any  $\sigma$ , can also be calculated from Eq. (2).

According to Eq. 5, the slopes of the lines in Fig. 6(b) should be equal to  $3k_1\Omega/b$ . Assuming  $k_1 = 2$ ,  $\Omega/b$  can thus be calculated. Note that, according to Eq. (5), the lines in Fig. 6(b) should go through the origin, when, in fact, they do not. The exact reason for this state of affairs is most probably due to the presence of other non-linear reversible strains that are not due to IKBs. Such strains were observed when polycrystalline Co samples were compressed.<sup>31</sup> However, this discrepancy is not believed to considerably affect the slopes.



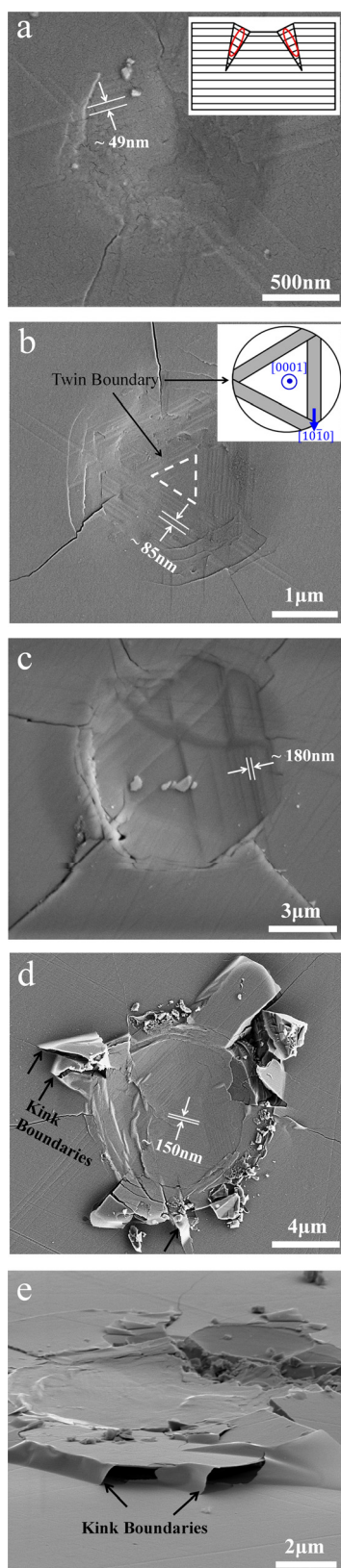


FIG. 7. (Color online) SEM images of NI mark on unirradiated sample made with the (a)  $1.4\ \mu\text{m}$  tip loaded to 20 mN after first cycle, (b)  $5\ \mu\text{m}$  tip loaded to 100 mN after first cycle, and  $21\ \mu\text{m}$  tip loaded to 550 mN after (c) 5 cycles and (d) 20 cycles; (e) same as (d) but tilted  $75^\circ$ . Note three-fold symmetry of the linear surface features best seen in (b) and (c). The top inset in (a) is a schematic of domains forming in the twins. Top inset in (b) shows three-fold symmetry of twins, which form in  $\text{LiNbO}_3$ , adapted from Ref. 48. The features with very sharp radii of curvature in (d) and (e) are kink boundaries.

The reversible dislocation density can, in turn, be calculated from Eq. (6). The calculated values for  $\sigma_t$ ,  $2\alpha$ ,  $N_k$ ,  $\Omega/b$ ,  $2\beta_x$ ,  $2\beta_y$ , and  $\rho$ , the latter three at 5 GPa, are listed in Table I.

## B. Microstructural observations

Despite the fact that all of the tips used were spherical, the indentation imprints in the SEM clearly exhibited three-fold symmetry (Fig. 7). The three-fold symmetry is clearest in Figs. 7(b) and 7(c). The widths of the domains for the  $1.4\ \mu\text{m}$ ,  $5\ \mu\text{m}$ , and  $21\ \mu\text{m}$ , shown in Figs. 7(a) to 7(d), respectively, were found to be a function of  $R$ .

## C. Irradiation damage

Almost all of the stopping power for the 2 MeV  $\text{He}^+$  ions in  $\text{LiTaO}_3$  is attributable to electronic stopping. Nuclear stopping only plays an appreciable role near the ion end-of-range (at depths from  $4.0\text{--}4.8\ \mu\text{m}$ ). The damage energy,  $\nu(E)$ , which is the fraction of the total energy ( $E = 2\ \text{MeV}$ ) that is consumed in ballistic damage events (i.e., kinematic scattering by atomic nuclei in the target) is only 0.0092 MeV or 0.46% of the primary ion energy.

The RBS spectra from the unirradiated and irradiated samples are shown in Fig. 8 and indicated that the un-irradiated sample was of a high quality. The spectrum did not change after irradiation (it was slightly higher, but within the statistical error of measurements), confirming that the defect concentration in the near surface region is small and below the sensitivity level. These RBS spectra correspond to a near surface region  $\sim 2\ \mu\text{m}$  thick.

## IV. DISCUSSION

Given that: a) Doukhan *et al.*<sup>6</sup> reported  $(10\bar{1}2)[10\bar{1}1]$  twins as the only deformation system in  $\text{LiTaO}_3$  during

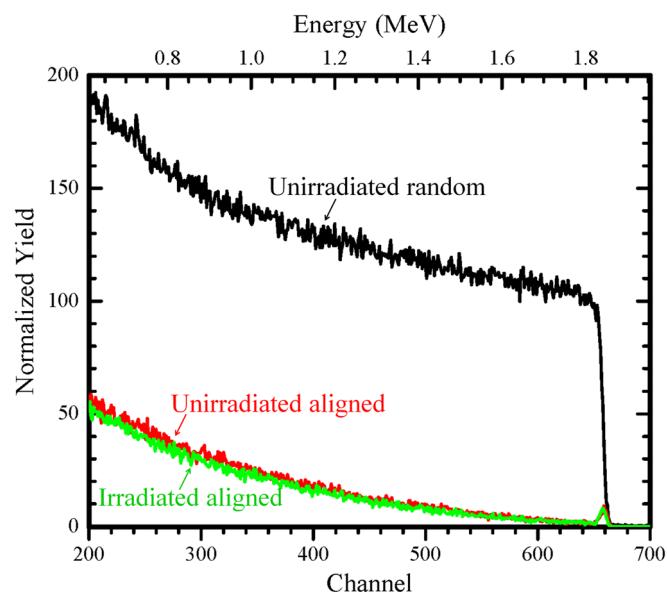


FIG. 8. (Color online) RBS spectra from unirradiated random, unirradiated aligned, and irradiated aligned. The  $\chi_{\min} = 1.5\%$  (ratio of aligned to random yield just below the surface peak) indicated very good quality of the unirradiated sample. The aligned spectrum did not change after irradiation because the concentration of defects in the near surface region is quite small.

compression along the c-axis; b) the twinning system in  $\text{LiTaO}_3$  is identical to that of  $\text{LiNbO}_3$ ;<sup>6</sup> c) the traces and steps shown in Fig. 7 are similar to those observed in  $\text{LiNbO}_3$ ;<sup>25</sup> and d) the three-fold symmetry of the indentation marks are very similar to those reported by Park *et al.*<sup>48–50</sup> in  $\text{LiNbO}_3$  (see inset in Fig. 7(b)), it is reasonable to conclude that the traces observed in Fig. 7 are due to the formation of  $(10\bar{1}2)[10\bar{1}1]$  twins.

In our previous paper,<sup>25</sup> we argued that, since the loading was along  $[0001]$ , the distance between the lines shown in Figs. 7(a), 7(b), 7(c), and 7(d) is the width of the domains,  $2\beta$ , and not their lengths,  $2\alpha$ . A schematic of what we believe happens is shown in the top inset in Fig. 7(a). There is no reason to believe things are different here. Also, shown in Figs. 7(d) and 7(e) are some exceedingly sharp bends that can *only* be due to kink boundaries, which is strong indirect evidence that kinking must be operative in this material.

Based on the results shown above and those listed in Table I, and by analogy with  $\text{LiNbO}_3$ , we conclude that  $\text{LiTaO}_3$  is a KNE solid. As discussed previously,<sup>7,12–14,16,18</sup> the deformation of KNE solids under cyclic spherical NI can be explained by invoking the formation and annihilation of spontaneously reversible IKB dislocation loops.

According to the results shown in Fig. 3, it is obvious that, after the first cycle, hysteretic loops – whose areas,  $W_d$ , get smaller until they reach a steady-state value that is no longer a function of cycling – evolve.<sup>7,9,12,13,18,25</sup> These fully reversible and reproducible loops are quite similar to those observed in other KNE solids. The different parameters, calculated from the nested loops, all yield reasonable results (Table I).

The resulting reversible dislocation densities (Table I) are comparable to heavily deformed metals<sup>28</sup> and are, again, reasonable, considering they are calculated at a stress of 5 GPa.<sup>25</sup> It is important to note that, despite the differences in the shape and size of the loops shown in Fig. 4(b), at comparable stresses,  $\rho$  is a weak function of R. The importance of this conclusion lies in the fact that the crystal responds to the applied stress by forming dislocation loops, whose total lengths per unit volume are more a function of  $\sigma$  than R.<sup>25</sup> Note, this conclusion is valid for the three tip sizes, even though the  $2\beta$  values for the 5  $\mu\text{m}$  indents do not match with those of the 1.4 and 21  $\mu\text{m}$  tips.

The  $\sigma_t$  values shown in Table I decrease with increasing R. As postulated in our previous work,<sup>25</sup> this is most prob-

ably due to the shrinking of domain size,  $2\alpha$ . For smaller R values, the domains are smaller and thus – from Eq. (1) – the threshold stresses should be larger, as observed (Fig. 6 and Table I).

When the NI stress-strain responses of the irradiated and un-irradiated surfaces are superimposed (not shown), they were, within the resolution of our experiments and experimental scatter, identical. Said otherwise, the irradiation did *not* affect the stress-strain curves either before, or after the yield points.

Further evidence that the irradiation had little effect on the response is shown in Fig. 5. The mean and standard deviation of the pop-in stresses for the irradiated sample was  $2.059 \pm 0.14$ ; that for the unirradiated sample was  $2.205 \pm 0.09$ . Clearly, these values with their uncertainties overlap. It follows that the difference we see in Fig. 5 cannot be significant. This is especially true since taking these values at face value implies that irradiation increased the pop-in stresses, a conclusion which is difficult to reconcile with our previous work on mica that showed that the pop-in stresses decreased with defect concentration.<sup>17</sup> The same is true here; it is difficult to argue for a mechanism where irradiation would somehow suppress the pop-in stresses.

The reason for this state of affairs is believed to be the mild nature of the irradiation. Using a modified Kinchin-Pease equation to estimate the number of displaced atoms per incident ion,<sup>51</sup> we find that the number of displaced atoms per ion is  $\sim 92$  (assuming the displacement threshold energy,  $E_d$ , for all target atoms – Li, Ta, and O – is given by  $E_d = 40$  eV, which is an arbitrary assumption often used as a reasonable guess for ceramics when there are no measured values available). The peak displacement damage dose is approximately 0.02 dpa at a target depth of  $\sim 4.6$   $\mu\text{m}$ . However, the average displacement damage dose is only about 0.001 dpa over the first 2  $\mu\text{m}$  of target depth.

In summary, over the first two microns of target depth, the 2 MeV  $\text{He}^+$  ions implanted to a fluence,  $\Phi = 1.67 \times 10^{15}$   $\text{He}/\text{cm}^2$ , produce only about one Frenkel pair per 1000 target atoms. About 99.9% of the ion stopping over this target volume is due to electronic stopping. Unless  $\text{LiTaO}_3$  is highly susceptible to radiolysis (i.e., permanent atomic displacements due to electronic excitations and bond breaking), then these irradiation conditions will produce little in the way of permanent point defects or atomic disorder. This would explain why no detectable changes in mechanical properties were observed in the NI experiments. In future experiments, ion fluences that will produce more ballistic damage over the first two microns will be used.

For reasons that are not entirely clear, twins are easier to nucleate when the sharper tips are used. This is best seen by the lack of pop-in stresses when the 1.4 and 5  $\mu\text{m}$  tips are used. With the 21  $\mu\text{m}$  tip, the strain energy has to reach a certain value before the twins are nucleated. This is an important observation that needs to be further looked into, since it signifies that the nucleation of twins depends on more than the stress under the indenter.

In our work on the MAX phases, we have shown that  $\Omega/b$  or the CRSS of the IKB dislocations is inversely proportional to the square root of the grain or domain size.<sup>10</sup>

TABLE I. Summary of various measured and calculated parameters as a function of R. The following was assumed:  $\gamma = 0.05$ ,  $w = b = 0.515$  nm,  $G = 96.8$  GPa,  $\nu = 0.25$ ,  $M = 2$ , and  $k_1 = 2$ .

Tip radius ( $\mu\text{m}$ )	1.4	5	21
$\sigma_t$ (GPa) (from Fig. 6(a))	$3.2 \pm 0.1$	$2 \pm 0.2$	$1.8 \pm 0.2$
$2\alpha$ (nm) (calculated)	$114 \pm 5$	$292 \pm 112$	$361 \pm 60$
$N_k \alpha^3$	0.45	0.78	1.78
$N_k$ ( $\text{m}^{-3}$ )	$2.2 \times 10^{21}$	$2.5 \times 10^{20}$	$3.0 \times 10^{20}$
$\Omega/b$ (MPa)	$1.3 \times 10^3$	$1.1 \times 10^3$	$0.7 \times 10^3$
$2\beta_x$ (nm) at 5 GPa	$44 \pm 2$	$113 \pm 40$	$140 \pm 22$
$2\beta_y$ (nm) at 5 GPa	$59 \pm 6$	$151 \pm 57$	$186 \pm 31$
$2\beta_y$ (nm) (Fig. 7. SEM image)	$49 \pm 5$	$90 \pm 25$	$180 \pm 40$
$\rho$ ( $\text{m}^{-2}$ ) at 5 GPa	$4 \times 10^{15}$	$3 \times 10^{15}$	$5 \times 10^{16}$

To check whether this is true, here we plotted  $\Omega/b$  versus  $1/\sqrt{2\alpha}$  (Fig. 9). A decent correlation was found. If one plots  $\Omega/b$  versus  $1/2\beta$ , measured directly from the SEM micrographs (see below), an even better correlation is found (Fig. 9). Since  $\alpha$  is proportional to  $\beta$ , this correlation again is consistent with  $\Omega/b$  values that follow a Hall-Petch like relationship. Lastly, one can also plot  $\Omega/b$  versus  $1/\sqrt{R}$ ; again the correlation is acceptable. Note that the correlation found in Fig. 9 is not a result of a circular argument, since  $\alpha$  is calculated from  $\sigma_t$  and the CRSSs are calculated from the totally independent measurements of  $W_d$  and  $\varepsilon_{NL}$ . The correlations between  $\Omega/b$  versus  $1/\sqrt{R}$  or  $1/\sqrt{2\beta}$  are, thus, also totally independent.

When  $\Omega/b$  is plotted versus  $1/\sqrt{R}$  for the LiNbO<sub>3</sub> single crystals,<sup>25</sup> – shown as a black dashed line in Fig. 9 – using the methodology used herein, the correlation is once again excellent. (The calculations of  $\Omega/b$  made in Ref. 25 made slightly different assumptions to reach different values of  $\Omega/b$ ). Not only is the correlation excellent, but the resulting line is almost parallel to that for LiTaO<sub>3</sub> (the line at extreme left in Fig. 9). This is an important result for the following reason: if one makes the reasonable assumption that the CRSSs of the IKB dislocations are proportional to  $c_{44}$ , then the ratio of CRSSs for LiTaO<sub>3</sub> and LiNbO<sub>3</sub> should be  $\approx 1.62$ . Gratifyingly, the ratio of CRSSs – for a given domain size denoted by the vertical dashed line – obtained from the results shown in Fig. 9 is  $\approx 1.6$ . Whether this is coincidental or not needs more work on other crystals with different  $c_{44}$  values, but is certainly consistent with the ideas proposed herein.

Comparing both calculated and measured values for  $2\beta_y$  in Table I shows that the calculated values from the model and measured values from SEM images for 1.4  $\mu\text{m}$  and 21  $\mu\text{m}$  are in good agreement with each other. For reasons that are unclear, for the 5  $\mu\text{m}$  indents, the calculated values differ from the measured ones. Also, the calculated length of the IKBs,  $2\alpha$ , for 1.4  $\mu\text{m}$ , 5  $\mu\text{m}$ , and 21  $\mu\text{m}$  indents are quite reasonable and scale with the indenter radii.

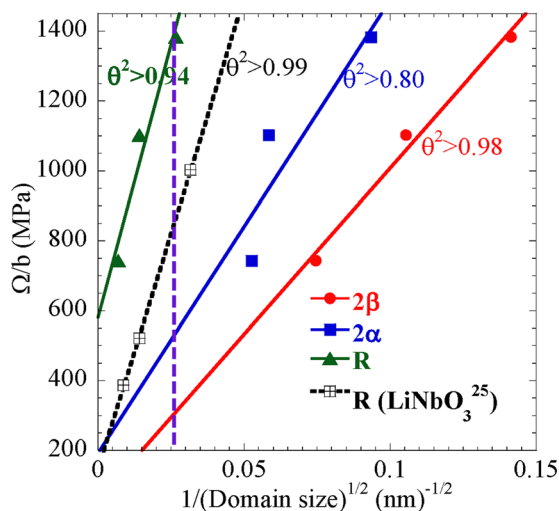


FIG. 9. (Color online) Hall-Petch-like correlation between the CRSS of the IKB dislocations ( $\Omega/b$ ) and  $1/\sqrt{\text{domain size}}$ , where the domain size is assumed to be  $2\alpha$ ,  $2\beta$ , or  $R$ . The black dashed inclined line represents  $\Omega/b$  vs  $1/\sqrt{R}$  for LiNbO<sub>3</sub> (see Ref. 25).

Based on the totality of our results, the following scenario for what happens under the spherical NI tips can be recreated. At pop-in for the 21  $\mu\text{m}$  indenter, or at the yield points for the other two tips, twins form. These twins, in turn, rotate basal planes into orientations that are more amenable for basal slip. Concomitantly, or as a result, the single crystal is fragmented into much smaller domains, with a size that scales with  $R$ . At a threshold stress – that is inversely proportional to the square root of the domain size – IKBs nucleate within these domains. The IKBs are fully reversible, and the to-and-fro motion of the IKB dislocations dissipates substantial amounts of energy.

Note that IKBs cannot form in single crystals because, once they become critical, they would simply run to the ends of the crystal and devolve into mobile dislocation walls.<sup>11</sup> Equation (1) – derived using a Griffith-like approach – is based on that scenario. IKBs can thus only form when there are grain, twin, or domain boundaries that confine them. During NI, these domains form during the first cycle, especially after pop-in events or yield points. It was expected that irradiation defects on the surface reduce the pop-in stress.

We note that the Vickers hardness values and the minima in the stress-strain curves after pop-ins or simply the yield points, if pop-ins are not present (Fig. 4(b)), are in excellent agreement. This is an important result since it indirectly confirms our methodology for converting NI load/displacement to NI stress-strain curves. The same observation was made in most of our other previous work.<sup>12,14,25</sup> The fact that the Berkovich modulus is also in good agreement with our value is another independent confirmation for our NI methodology.

Lastly, it is worth emphasizing that, given the many simplifying assumptions made in our KNE model, such as assuming a uniform uniaxial stress state, which is far from what is happening during NI, to the definition of strain to be  $a/R$  and other simplifying assumptions, the agreement between theory and experiment has to be considered excellent. One reason for this state of affairs is that the calculation of contact stresses is reasonably straightforward. Moreover, since the non-linear strains are small, the results obtained are a weak function of the exact definition of strain. These comments notwithstanding, it is hereby acknowledged, as noted above, that the absolute values of CRSS calculated herein have to be taken with a large grain of salt because of all the aforementioned simplifications, etc.

## V. CONCLUSIONS

The deformation response of C-plane LiTaO<sub>3</sub> single crystals was studied using spherical indenters with three different radii. When the load/displacement results are converted to NI stress-strain curves, we conclude that:

- During the first NI cycle, two regimes are observed: a linear elastic regime followed by a plastic regime, in which strain-hardening is observed. For the smaller tips, plastic deformation is accompanied by (10 $\bar{1}2$ ) twins. In the case of the 21  $\mu\text{m}$  indenter, the elastic regime was separated from the plastic regime by pop-ins. At the pop-ins, twins are nucleated.



- (b) The elastic moduli determined from  $S$  versus  $a$  curves of the 1.4  $\mu\text{m}$  and 5  $\mu\text{m}$  tips was  $205 \pm 5\text{ GPa}$ . The corresponding Berkovich modulus is  $207 \pm 3\text{ GPa}$ .
- (c) No noticeable effect of the irradiation was observed on the NI results of the sample. The main reason for this state of affairs is believed to be the mildness of the irradiation conditions.
- (d) When spherical indenters were repeatedly loaded to a given maximum load, fully reversible, reproducible hysteresis loops are obtained. The  $\Omega/b$  values calculated from the model were inversely proportional to the square root of the domain size.
- (e) The ratio of the CRSSs for  $\text{LiNbO}_3$  and  $\text{LiTaO}_3$  determined from our IKB-based microscale model were found to be roughly equal to the ratios of the shear moduli of these two compounds.

## ACKNOWLEDGMENTS

This work was supported by the Army Research Office (No. DAAD19-03-1-0213).

- <sup>1</sup>E. D. Palik, *Handbook of Optical Constants of Solids* (Academic, San Diego, 1998), Vol. 3, p. 777.
- <sup>2</sup>V. G. Dmitriev, G. G. Gurzadyan, and D. N. Nikogosyan, *Handbook of Nonlinear Optical Crystals*, Vol. **64**, (Springer, New York, 1999).
- <sup>3</sup>G. D. B. A. Ashkin, J. M. Dziedzic, and R. G. Smith, *Appl. Phys. Lett.* **9**, 72 (1966).
- <sup>4</sup>K. Mizuuchi, K. Yamamoto, and T. Taniuchi, *Appl. Phys. Lett.* **59**, 1538 (1991).
- <sup>5</sup>G. Assanto, G. Stegeman, M. Sheikbahae, and E. Vanstryland, *Appl. Phys. Lett.* **62**, 1323 (1993).
- <sup>6</sup>J. C. Doukhan, P. Cordier, and N. Doukhan, in *Proceedings of the 43rd Annual Symposium on Frequency Control*, Denver, CO, USA, 31 May–2 June 1989, pp. 497–508.
- <sup>7</sup>M. W. Barsoum, A. Murugaiah, S. R. Kalidindi, and T. Zhen, *Phys. Rev. Lett.* **92**, 255508 (2004).
- <sup>8</sup>M. W. Barsoum, T. Zhen, A. Zhou, S. Basu, and S. R. Kalidindi, *Phys. Rev. B* **71**, 134101 (2005).
- <sup>9</sup>A. G. Zhou, M. W. Barsoum, S. Basu, S. R. Kalidindi, and T. El-Raghy, *Acta Mater.* **54**, 1631 (2006).
- <sup>10</sup>M. W. Barsoum and S. Basu, in *Encyclopedia of Materials Science and Technology*, edited by R. W. C. K. H. J. Buschow, M. C. Flemings, B. Ilshner, E. J. Kramer, S. Mahajan, and P. Veyssiere (Elsevier, Oxford, 2010), p. 1.
- <sup>11</sup>F. C. Frank and A. N. Stroh, *Proc. Phys. Soc. London* **65**, 811 (1952).
- <sup>12</sup>S. Basu and M. W. Barsoum, *J. Mater. Res.* **22**, 2470 (2007).
- <sup>13</sup>S. Basu, M. W. Barsoum, and S. R. Kalidindi, *J. Appl. Phys.* **99**, 063501 (2006).
- <sup>14</sup>S. Basu, M. W. Barsoum, A. D. Williams, and T. D. Moustakas, *J. Appl. Phys.* **101**, 083522 (2007).
- <sup>15</sup>B. J. Kooi, R. J. Poppen, N. J. M. Carvalho, J. T. M. De Hosson, and M. W. Barsoum, *Acta Mater.* **51**, 2859 (2003).
- <sup>16</sup>A. Murugaiah, M. W. Barsoum, S. R. Kalidindi, and T. Zhen, *J. Mater. Res.* **19**, 2194 (2004).
- <sup>17</sup>S. Basu, A. Zhou, and M. W. Barsoum, *J. Struct. Geol.* **31**, 791 (2009).
- <sup>18</sup>M. W. Barsoum, A. Murugaiah, S. R. Kalidindi, T. Zhen, and Y. Gogotsi, *Carbon* **42**, 1435 (2004).
- <sup>19</sup>E. G. Herbert, G. M. Pharr, W. C. Oliver, B. N. Lucas, and J. L. Hay, in *On the Measurement of Stress-Strain Curves by Spherical Indentation* (Elsevier, San Diego, 2001), p. 331.
- <sup>20</sup>W. C. Oliver and G. M. Pharr, *J. Mater. Res.* **19**, 3 (2004).
- <sup>21</sup>M. Suganuma and M. V. Swain, *J. Mater. Res.* **19**, 3490 (2004).
- <sup>22</sup>A. J. Bushby, *Nondestruct. Test. Eval.* **17**, 213 (2001).
- <sup>23</sup>S. Basu, A. Moseson, and M. W. Barsoum, *J. Mater. Res.* **21**, 2628 (2006).
- <sup>24</sup>A. J. Moseson, S. Basu, and M. W. Barsoum, *J. Mater. Res.* **23**, 204 (2008).
- <sup>25</sup>S. Basu, A. G. Zhou, and M. W. Barsoum, *J. Mater. Res.* **23**, 1334 (2008).
- <sup>26</sup>R. Buchs, S. Basu, O. A. Elshrief, R. Coward, and M. W. Barsoum, *J. Appl. Phys.* **105**, 093540 (2009).
- <sup>27</sup>I. C. Albayrak, S. Basu, A. Sakulich, O. Yeheskel, and M. W. Barsoum, *J. Am. Ceram. Soc.* **93**, 2028 (2010).
- <sup>28</sup>D. Hull, *Introduction to Dislocations* (Pergamon Press, Oxford, 1965).
- <sup>29</sup>A. G. Zhou, S. Basu, and M. W. Barsoum, *Acta Mater.* **56**, 60 (2008).
- <sup>30</sup>A. G. Zhou and M. W. Barsoum, *Metall. Mater. Trans. A* **40A**, 1741 (2009).
- <sup>31</sup>A. G. Zhou, D. Brown, S. Vogel, O. Yeheskel, and M. W. Barsoum, *Mater. Sci. Eng., A* **527**, 4664 (2010).
- <sup>32</sup>R. E. Reed-Hill, E. P. Dahlberg, and W. A. Slippy, Jr., *Trans. Am. Inst. Min., Metall. Pet. Eng.* **233**, 1766 (1965).
- <sup>33</sup>N. Li, M. S. Martin, O. Anderoglu, A. Misra, L. Shao, H. Wang, and X. Zhang, *J. Appl. Phys.* **105**, 123522 (2009).
- <sup>34</sup>H. Trinkaus and W. G. Wolfer, *J. Nucl. Mater.* **122**, 552 (1984).
- <sup>35</sup>J. N. Mitchell, R. Devanathan, N. Yu, K. E. Sickafus, C. J. Wetteland, V. Gopalan, M. A. Nastasi, and K. J. McClellan, *Nucl. Instrum. Methods Phys. Res. B* **141**, 461 (1998).
- <sup>36</sup>C. J. Wetteland, K. E. Sickafus, V. Gopalan, J. N. Mitchell, T. Hartmann, M. A. Nastasi, C. J. Maggiore, J. R. Tesmer, and T. E. Mitchell, *Mater. Res. Soc. Symp. Proc.* **504**, 159 (1999).
- <sup>37</sup>J. Li, X. M. Zhou, W. J. Zhu, and F. Q. Jing, *J. Appl. Phys.* **102**, 083503 (2007).
- <sup>38</sup>J. Lindhard and M. Scharff, *Phys. Rev.* **124**, 128 (1961).
- <sup>39</sup>J. Lindhard, M. Scharff, and H. E. Schiott, *K. Dan. Vidensk. Selsk. Mat. Fys. Medd.* **33**, 39 (1963).
- <sup>40</sup>J. Lindhard, V. Nielsen, and M. Scharff, *K. Dan. Vidensk. Selsk. Mat. Fys. Medd.* **36**, 32 (1968).
- <sup>41</sup>J. Lindhard, V. Nielsen, M. Scharff, and P. V. Thomsen, *K. Dan. Vidensk. Selsk. Mat. Fys. Medd.* **33**, 1 (1963).
- <sup>42</sup>M. W. Barsoum, T. Zhen, S. R. Kalidindi, M. Radovic, and A. Murugaiah, *Nature Mater.* **2**, 107 (2003).
- <sup>43</sup>J. G. Gualtieri, J. A. Kosinski, and A. Ballato, *IEEE Trans. Ultrason. Ferroelectr. Freq. Control* **41**, 53 (1994).
- <sup>44</sup>V. Bornand, P. Papet, and E. Philpott, *Thin Solid Films* **304**, 239 (1997).
- <sup>45</sup>D. W. Brown, S. R. Agnew, S. P. Abeln, W. R. Blumenthal, M. A. M. Bourke, M. C. Mataya, C. N. Tome, and S. C. Vogel, in *The Role of Texture, Temperature, and Strain Rate in the Activity of Deformation Twinning* (Trans Tech, Switzerland, 2005), p. 1037.
- <sup>46</sup>B. Clausen, C. N. Tome, D. W. Brown, and S. R. Agnew, *Acta Mater.* **56**, 2456 (2008).
- <sup>47</sup>E. J. Freise and A. Kelly, *Proc. R. Soc. London, Ser. A* **264**, 269 (1961).
- <sup>48</sup>B. M. Park, K. Kitamura, and Y. Furukawa, in *Relations Between Ferroelectric Polarization and Mechanical Twinning in Stoichiometric Lithium Niobate Single Crystal* (Korean Phys. Soc., South Korea, 1998), p. 789.
- <sup>49</sup>B. M. Park, K. Kitamura, Y. Furukawa, and J. Yangyang, *J. Am. Ceram. Soc.* **80**, 2689 (1997).
- <sup>50</sup>B. M. Park, K. Kitamura, K. Terabe, Y. Furukawa, Y. Ji, and E. Suzuki, *J. Cryst. Growth* **180**, 101 (1997).
- <sup>51</sup>M. J. Norgett, M. T. Robinson, and I. M. Torrens, *Nucl. Eng. Des.* **33**, 50 (1975).